Opt Quant Electron (2009) 41:645–652
DOI 10.1007/s11082-010-9372-4

The analysis of factors limiting the maximum output power of broad-area laser diodes

H. Wenzel · P. Crump · A. Pietrzak · C. Roder · X. Wang · G. Erbert

Received: 5 October 2009 / Accepted: 11 February 2010 / Published online: 27 February 2010
© Springer Science+Business Media, LLC. 2010

Abstract The causes for the saturation of both the continuous-wave and the pulsed output power of broad-area laser diodes driven at very high currents are investigated experimentally and theoretically. The decrease of the gain due to self-heating under continuous-wave operation and spectral holeburning under pulsed operation as well as hetero-barrier carrier leakage and longitudinal spatial holeburning are the dominant mechanisms limiting the maximum achievable output power.

Keywords Simulation · Longitudinal spatial holeburning · Spectral holeburning

1 Introduction

High-power laser diodes are the root source of optical energy in all high performance laser systems. Broad-area diode lasers (either as single emitters or in bars) are in wide-spread application in part because of their ease of fabrication. In recent years, their output power was driven to higher and higher values by steadily increasing the efficiency. In principle the maximum achievable power is limited by the damage threshold of the semiconductor crystal (catastrophic optical damage, COD), either within the laser cavity or at the facets. However, different measures like the reduction of the power density by broadening the optical waveguide (Erbert et al. 2008), the improvement of the crystal quality (Bugge et al. 2007) and special facet treatments (Ressel et al. 2005) significantly extended the COD power. Thus increasingly physical effects like self-heating (Crump et al. 2009), carrier leakage (Pietrzak et al. 2009) and gain compression (Slipchenko et al. 2006) limit the achievable power.

H. Wenzel (✉) · P. Crump · A. Pietrzak · C. Roder · X. Wang · G. Erbert
Ferdinand-Braun-Institut für Höchstfrequenztechnik, Gustav-Kirchhoff-Str. 4, 12489 Berlin, Germany
e-mail: wenzel@fbh-berlin.de

C. Roder
Paul-Drude-Institut für Festkörperelektronik, Hausvogteiplatz 5-7, 10117 Berlin, Germany

New detailed comparisons of simulation and experiment allow the relative importance of different physical effects to be inferred. Specifically, in this paper we present results of two-dimensional (vertical-longitudinal) simulations of the maximum achievable power in BA lasers. The simulations accurately describe transverse carrier transport, heat flow, and wave-guiding taking into account hetero-barrier leakage, longitudinal spatial holeburning (LSH) and spectral holeburning (SHB). Lateral effects like current spreading, filamentation and thermal lensing as well as spectral effects are ignored. We consider both continuous-wave (CW) operation and pulsed operation, where the self-heating of the lasers can be neglected, and compare the results to measurements.

2 Model

A schematic three-dimensional view of simulation domain and coordinate system is shown in Fig. 1. The longitudinal direction is given by the z axis and the transverse plane by the xy plane. In this paper, any dependencies in the lateral (y) direction are neglected and the simulation in the transverse plane is restricted to the vertical (x) direction. This is appropriate for a BA laser, where on the average optical field, carrier densities and temperature can be assumed to be constant along the lateral direction. In fact, in this paper output power and current are scaled corresponding to a lateral width of $W = 100\ \mu\text{m}$.

The simulations are based on the “Treat Power as a Parameter” (TPP) method as explained in Wünsche et al. (1993) and Wenzel and Erbert (1996). In Fabry-Perot lasers the forward and backward propagating optical power P^+ and P^- are solutions of the equations

$$\pm \frac{dP^\pm}{dz} = \frac{g_m(U, P)}{1 + \frac{P}{P_s}} P^\pm \tag{1}$$

subject to the boundary conditions

$$P^+(0) = R_0 P^-(0) \quad \text{and} \quad P^-(L) = R_L P^+(L), \tag{2}$$

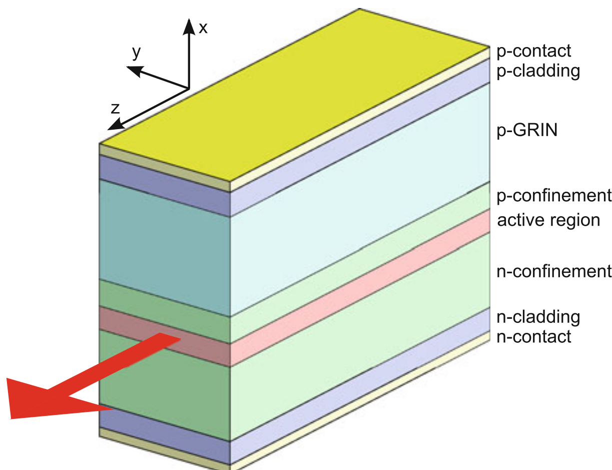

Fig. 1 Schematic three-dimensional view of the device under investigation

where R_0 and R_L are the reflection coefficients at the facets, $P = P^+ + P^-$ is the total power and P_s is a saturation power describing phenomenologically gain compression caused by spectral holeburning and carrier heating (denoted by SHB) (Wang and Schweizer 1997). A value of P_s is given at the end of Sect. 3. We should mention, that in a more correct treatment gain compression effects have to be directly included in the local gain g which enters Eq. 3 below and the rate of stimulated recombination.

The modal gain g_m is twice the imaginary part of the propagation constant β which is obtained as a solution of the transverse waveguide equation for the optical field E

$$\left[\frac{d^2}{dx^2} + \frac{4\pi^2}{\lambda^2}\varepsilon(n, p, T, x) - \beta^2\right] E(x) = 0, \tag{3}$$

where

$$\varepsilon = \left[\tilde{n} + \frac{i\lambda(g - \alpha)}{4\pi}\right]^2 \tag{4}$$

is the complex dielectric function with λ being the wavelength, $\tilde{n}$ the refractive index, g the local gain and α the local absorption coefficient. The different nontrivial solutions of Eq. 3 subject to proper boundary conditions are the transverse modes of the laser. In this paper, we consider only the 0th order (vertical) mode.

The electron and hole densities n and p as well as the temperature distribution T are solutions of the transverse Poisson, drift-diffusion and heat-flow equations which are solved by the tool WIAS-TeSCA (Bandelow et al. 2005). As a result, g_m is obtained as a function of the applied bias U and the local power P and stored in a look-up table. LSH is included automatically via the power dependence of g_m in Eq. 1. If g_m is evaluated at the average power in the cavity and if $P_s \to \infty$, the usual model neglecting LSH and SHB is recovered.

The equations are supplemented by proper boundary conditions. The optical field E is assumed to vanish at the upper and lower boundary. The contacts are assumed to be Ohmic, so that the electrochemical potentials of electrons and holes are set to $-U$ at the p-contact and to zero at the n-contact. A mathematical formulation can be found in Ref. Bandelow et al. (2005).

The heat flow equation is solved subject to the boundary condition

$$\nu\kappa_L \frac{dT}{dx} = h\,[T_s - T] \tag{5}$$

where $\nu = \pm 1$ is the normal unit vector, κ_L is the thermal conductivity of the lattice and $T_s = 300$ K is the heat sink temperature. The heat transfer coefficient h models the heat flow to the exterior region and is chosen as follows. For CW operation, $h = 0$ holds at the boundary opposite to the heatsink and h is fitted to the experimentally determined temperature rise in active region at the boundary adjacent to the heatsink. For pulsed operation, h is set to a very large number at all boundaries, which implies that $T = T_s$ holds everywhere.

Most of the parameters entering the simulation are standard values extracted from different references (Adachi 1985; van de Walle 1989; Adachi 1993; Bhattacharya 1993; Madelung 1996; Guden and Piprek 1996). In what follows we give the dependencies of some parameters on the carrier densities and the temperature. In all equations $T_0 = 300$ K is a reference temperature and n_0, p_0 are the equilibrium carrier densities.

- refractive index and energy gaps: independent of carrier densities and temperature
- linear recombination lifetimes $\tau_n = \tau_p = 3$ ns
- rate of radiative recombination

$$R_{\rm rad} = B\left[\frac{T}{T_0}\right]^{-\gamma_B}[np - n_0p_0] \quad \text{with } B = 10^{-10}\ \text{cm}^3\text{s}^{-1},\ \gamma_B = 1$$

– rate of Auger recombination

$$R_{\rm Aug} = \left[C_n \mathrm{e}^{\frac{E_a^n}{kT_0}-\frac{E_a^n}{kT}} n + C_p \mathrm{e}^{\frac{E_a^p}{kT_0}-\frac{E_a^p}{kT}} p\right][np - n_0p_0]$$
$$\text{with} \quad C_n = C_p = 2\times 10^{-30}\ \text{cm}^6\text{s}^{-1},\ E_a^n = E_a^p = 0.1\ \text{eV}$$

– free carrier absorption

$$\alpha_{\rm fc} = f_{\rm cn}\left[\frac{T}{T_0}\right]^{\gamma^{\rm cn}} n + f_{\rm cp}\left[\frac{T}{T_0}\right]^{\gamma^{\rm cp}} p$$
$$\text{with} \quad f_{\rm cn} = 4\times 10^{-18}\ \text{cm}^2,\ f_{\rm cp} = 12\times 10^{-18}\ \text{cm}^2,\ \gamma_{\rm cn} = 1,\ \gamma_{\rm cp} = 2$$

– inverse mobilities: same temperature dependence as free carrier absorption
– optical gain

$$g(n,p) = g_0\cdot\left[\exp\left(\frac{F_n - F_p - E_g}{kT}\right) - 1\right]\cdot\frac{1}{1+\exp(\frac{F_n-E_c}{kT})}\cdot\frac{1}{1+\exp(\frac{E_v-F_p}{kT})}$$

with E_c, E_v conduction and valence band-edge energies,
$E_g = E_c - E_v$ energy gap,
F_n, F_p electron and hole quasi-Fermi energies
and $g_0 = 4{,}000\ \text{cm}^{-1}$ obtained from microscopic gain calculation
and validated by cavity-length dependent measurements of the threshold current

3 Results

The layer sequence, thicknesses and ionized doping densities of the structure under study are collected in Table 1. The epitaxial layer structure was grown on a n-GaAs substrate. The emission wavelength is $\lambda \approx 1{,}065$ nm. Cavity length and stripe width are $L = 4$ mm and $W = 100\ \mu$m, respectively, and the facet reflectivities are $R_0 = 0.01$ and $R_L = 0.95$. For CW operation, the laser diode was mounted p-down on a conductively cooled package with CuW as submount.

The transverse profiles of band-edge energies, quasi-Fermi energies and carrier densities are shown in Fig. 2 computed slightly below threshold ($I = 700$ mA). In the vicinity of the active region the band-edge and Fermi energies are almost flat. The presence of the GRIN, approximated by 4 layers here, is also clearly visible.

Figure 3 shows the measured and simulated power-current characteristics under CW and pulsed, respectively, operation of two laser diodes. Experimentally, a maximum CW output power of $P = 13$ W limited by thermal rollover and a maximum pulsed output power of $P = 90$ W limited by the current driver were achieved. The reason for the rollover can be seen from Fig. 4 which shows the transverse profiles of band-edge energies, quasi-Fermi energies and carrier densities. First, due to the decrease of the gain caused by internal self-heating the carrier densities in the QWs and as a consequence also the carrier densities in the confinement layers increase. Second, the voltage drop in the p-doped layers manifests in a bending of the quasi-Fermi energy of the holes and leads as a consequence to a bending of the band-edge energies. This causes a correspondingly linear rise of the electron density with increasing

Table 1 Layer sequence, thicknesses d and ionized doping densities C of the structure under study

Layer	Compound	Thickness d/nm	Doping $C/10^{18}$ cm^{-3}
Cladding	p-$Al_{0.25}Ga_{0.75}As$	25	−2
GRIN	p-GaAs → p-$Al_{0.25}Ga_{0.75}As$	1,500	−0.1 → −2
Confinement	p-GaAs	700	−0.05
		100	−0.01
Spacer	GaAs	10	
QW	$In_{0.29}Ga_{0.71}As$	7	
Barrier	GaAs	50	
QW	$In_{0.29}Ga_{0.71}As$	7	
Barrier	GaAs	50	
QW	$In_{0.29}Ga_{0.71}As$	7	
Barrier	GaAs	50	
QW	$In_{0.29}Ga_{0.71}As$	7	
Spacer	GaAs	10	
Confinement	n-GaAs	1,300	0.01
		300	0.1
		200	0.2
		100	0.5
Cladding	n-$Al_{0.25}Ga_{0.75}As$	100	0.5
		200	1

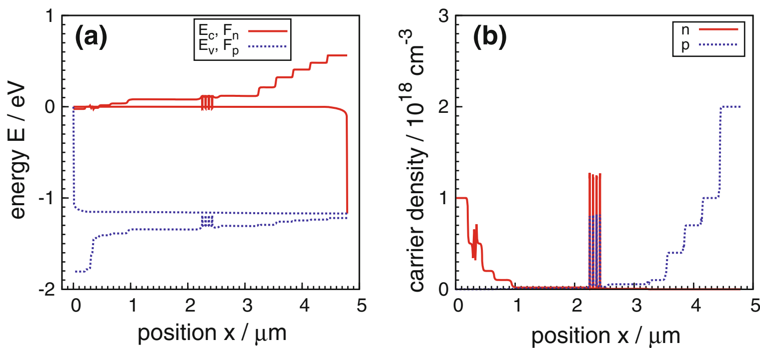

Fig. 2 Transverse profiles of **a** conduction and valence band-edge energies as well as quasi-Fermi energies and **b** electron and hole densities slightly below threshold (I = 700 mA)

distance from the QWs. The accumulated minority carrier densities give rise to increased non-stimulated recombination and free-carrier absorption.

However, as Fig. 3 reveals, good agreement between measurement and simulation is achieved only if LSH is included. Figure 5 shows the profiles of the the total power P and modal gain g_m as function of the longitudinal position z. LSH leads to a more rapid growth of the power in the vicinity of the rear facet at $z = 4$ mm where the gain is large and to a reduced increase of the power in the vicinity of the front facet at $z = 0$ where the gain approaches transparency. At the end this leads to a reduced output power. If LSH is neglected, the gain is

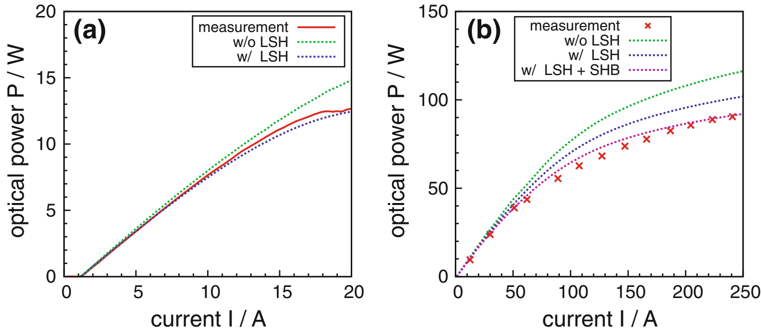

Fig. 3 Power-current characteristics for **a** CW and **b** pulsed operation. Solid lines and crosses represent experimental results, dashed lines theoretical results

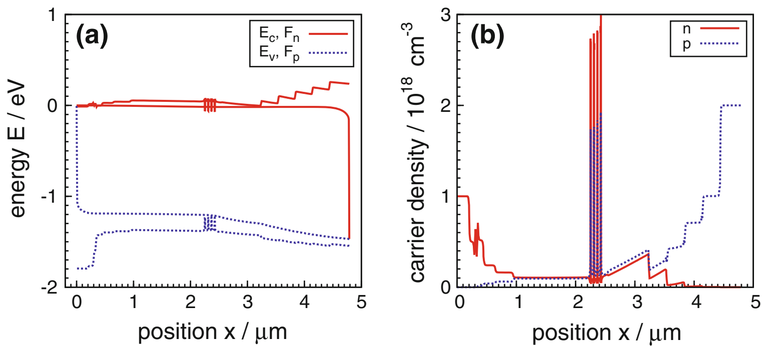

Fig. 4 CW transverse profiles of **a** conduction and valence band edges as well as quasi-Fermi energies and **b** electron and hole densities at a power of $P = 15$ A beyond roll-over (without LSH)

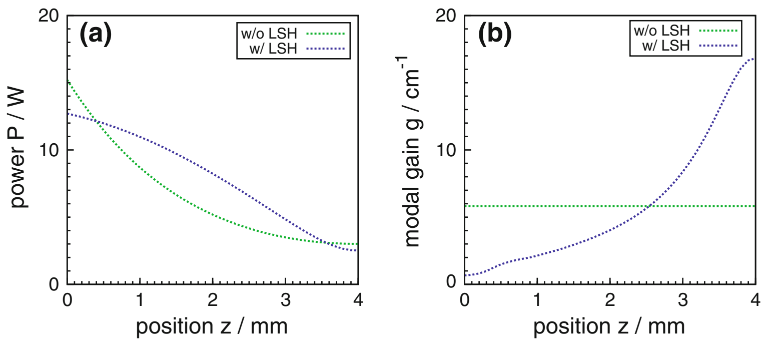

Fig. 5 Longitudinal profiles of **a** optical power and **b** modal gain for the cases with and without longitudinal spatial holeburning for a current of $I = 20$ A

constant across the cavity which leads to an almost exponential growth of the power towards the front facet.

Under operation with short current pulses (300 ns pulse width), self-heating can almost be neglected and much higher power levels can be reached. Nevertheless, the output power of $P = 90$ W obtained at a current of $I = 240$ A is smaller than expected from the slope

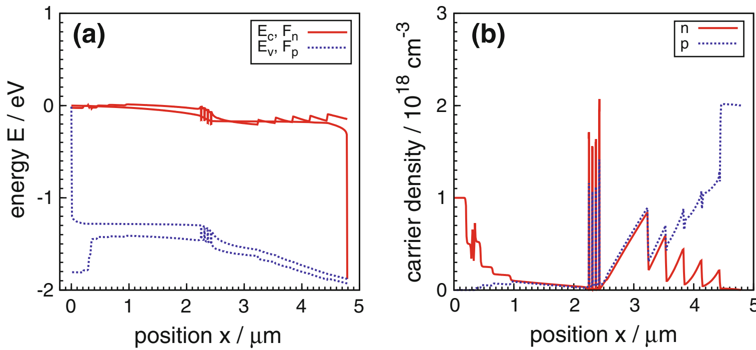

Fig. 6 Pulsed transverse profiles of **a** conduction and valence band-edge energies as well as quasi-Fermi energies and **b** electron and hole densities at a power of $P = 100$ W (without LSH and SHB)

efficiency $S = 0.9$ W/A determined at lower power levels. Even if LSH is neglected, already a decrease of the slope efficiency above an output power of $P = 50$ W is obtained in the simulation. The reason for this decrease can be seen from Fig. 6 which shows the transverse profiles of band-edge energies, quasi-Fermi energies and carrier densities. The voltage drop in both the n- and p-doped layers manifests in a bending of the quasi-Fermi energies of electrons and holes, respectively, and leads as a consequence to a bending of the corresponding band-edge energies. This causes a linear rise of the electron density in the p-confinement layer and even in the GRIN and a weaker rise of the hole density in the n-confinement layer with increasing distance from the QWs.

The strong reduction of the slope observed experimentally can only be reproduced if additionally to LSH gain compression due to SHB and other non-linear effects is taken into account. In order to match the experimental results, a saturation power of $P_s = 300$ W (for a lateral width of $W = 100\,\mu$m) has been chosen. This value corresponds to a gain compression factor of

$$\varepsilon_{SHB} = \frac{dW}{\Gamma}\frac{hc}{\lambda}\frac{c}{n_g}P_s^{-1} \approx 8 \times 10^{-24}\ \mathrm{m}^3$$

assuming $d = 0.028\,\mu$m, $W = 100\,\mu$m, $\Gamma = 0.02$, $\lambda = 1\,\mu$m, $n_g = 3.6$, which is at the lower limit of the values given in Wang and Schweizer (1997).

4 Conclusion

We achieved good agreement between measured and simulated light–current characteristics of high-power broad-area laser diodes using a drift–diffusion based numerical model. Longitudinal spatial holeburning and spectral holeburning (the later in case of pulsed operation only) must be taken into account. To a large extent, band bending and accumulation of minority carriers in bulk layers are responsible for thermal-rollover and power saturation. In order to further increase the output power the heating must be reduced, the band gaps of the bulk layers must be enlarged and the gain profile along the cavity must be homogenized.

Acknowledgements This work was funded by BMBF project "Grundlagen für Diodenlaser der nächsten Leistungsgeneration" (GRUNDILG) Förderkennzeichen 13 N 9154.

References

Adachi, S.: Gaas, AlAs, AlGaAs: material parameters for use in research and device applications. J. Appl. Phys. **58**(3), R1–R29 (1985)

Adachi, S. (ed.): Properties of Aluminium Gallium Arsenide. IET, Exeter (1993)

Bandelow, U., Gajewski, H., Hünlich, R.: Fabry-Perot lasers: thermodynamics-based modeling. In: Piprek, J. (ed.) Optoelectronic Devices—Advanced Simulation and Analysis, pp. 63–85. Springer, New York (2005)

Bhattacharya, P. (ed.): Properties of Lattice-Matched and Strained Indium Gallium Arsenide. IET, Exeter (1993)

Bugge, F., Zeimer, U., Staske, R., Sumpf, B., Erbert, G., Weyers, M.: MOVPE growth optimization for laser diodes with highly strained InGaAs MQWs. J. Cryst. Growth **298**, 652–657 (2007)

Crump, P., Blume, G., Paschke, K., Staske, R., Pietrzak, A., Zeimer, U., Einfeldt, S., Ginolas, A., Bugge, F., Häusler, K., Ressel, P., Wenzel, H., Erbert, G.: 20W continuous wave reliable operation of 980nm broad-area single emitter diode lasers with an aperture of 96μm. Proc. SPIE **7198**, 719,814 (2009)

Erbert, G., Bugge, F., Eppich, B., Fricke, J., Hasler, K.H., Paschke, K., Pietrzak, A., Wenzel, H., Tränkle, G.: High brightness diode lasers with very narrow vertical divergence. Proc. SPIE **6909**, 69,090P (2008)

Guden, M., Piprek, J.: Material parameters of quaternary III–V semiconductors for multilayer mirrors at 1.55 μm wavelength. Modelling Simul. Mater. Sci. Eng. **4**, 349–357 (1996)

Madelung, O. (ed.): Semiconductors-Basic Data. Springer, Berlin (1996)

Pietrzak, A., Crump, P., Wenzel, H., Staske, R., Erbert, G., Tränkle, G.: 55 W peak power from 1,100 nm wavelength 60 μm broad-area laser diodes enabled by reduced carrier accumulation in the waveguide. Semicond. Sci. Technol. **24**, 035,020 (2009)

Ressel, P., Erbert, G., Zeimer, U., Häusler, K., Beister, G., Sumpf, B., Klehr, A., Tränkle, G.: Novel passivation process for the mirror facets of Al-free active-region high-power semiconductor diode lasers. IEEE Photon Techn. Lett. **17**, 962–964 (2005)

Slipchenko, S.O., Sokolova, Z.N., Pikhtin, N.A., Borschev, K.S., Vinokurov, D.A., Tarasov, I.S.: Finite time of carrier energy relaxation as a cause of optical-power limitation in semiconductor lasers. Semiconductors **40**, 990 (2006)

van de Walle, C.G.: Band lineups and deformation potentials in the model-solid theory. Phys. Rev. B **39**(3), 1871–1883 (1989)

Wang, J., Schweizer, H.: A quantitative comparison of the classical rate-equation model with the carrier heating model on dynamics of the quantum-well laser. IEEE J. Quantum Electron **33**, 1350–1358 (1997)

Wenzel, H., Erbert, G.: Simulation of single-mode high-power semiconductor lasers. Proc. SPIE **2693**, 418 (1996)

Wünsche, H., Bandelow, U., Wenzel, H.: Calculation of combined lateral and longitudinal spatial hole burning in $\lambda/4$ shifted DFB lasers. IEEE J. Quantum Electron **17**, 1751–1760 (1993)